Materials Advances

ROYAL SOCIETY OF CHEMISTRY

PAPER

View Article Online
View Journal | View Issue

Cite this: *Mater. Adv.*, 2025, 6, 1119

Influence of alkali metal ions on the defect induced photoluminescence properties of double tungstate compounds $ACe(WO_4)_2$ (A = Li, Na, K): experimental and *ab initio* theoretical study†

Nibedita Haldar *[a] and Tanmoy Mondal[b]

Defect-induced alkali-metal cerium double tungstate compounds, $ACe(WO_4)_2$ (where A = Li, Na, K), have been synthesized through a trisodium citrate-based hydrothermal process. The influence of alkali-metal ions on the local structure of $ACe(WO_4)_2$ has been explored using various methods, including the Rietveld technique for powder X-ray diffraction (XRD), scanning electron microscopy (SEM), and transmission electron microscopy (TEM). Although the $ACe(WO_4)_2$ compounds exhibit similar transitions, they differ in luminescent intensity. Notably, in the case of the alkali metal Na, the material displays a larger crystal compactness due to its comparable ionic radii with Ce^{3+}. This proximity indicates lower distortion. Conversely, Li and K possess significantly different ionic radii from Ce^{3+}, leading to pronounced crystal distortion. The $ACe(WO_4)_2$ materials show emissions in blue and green spectra, including blue I (439 nm), blue II (462 nm), blue III (487 nm), and green (531 nm). The blue I emission is attributed to the 5d → 4f transition within the CeO_8 polyhedra, whereas the blue III emission arises from the same transition within CeO_7 polyhedra. The blue II and green emissions result from the formation of CeO_6 polyhedra. Additionally, *ab initio* calculations employing density functional theory reveal that the valence and conduction bands are composed of O 2p and O 2p–Ce 5d hybridization, respectively. Notably, the $5d_{xy}$, $5d_{xz}$, $5d_{yz}$, $5d_{x^2-y^2}$, and $5d_{xz}$, $5d_{x^2-y^2}$ orbitals significantly contribute to the 5d–4f transition within CeO_7 and CeO_6 polyhedra, respectively. The resulting Commission Internationale de l'Éclairage (CIE) coordinates in the blue region, coupled with a correlated color temperature (CCT) of approximately 7800 K, suggest that $ACe(WO_4)_2$ materials hold promise for applications in cold solid-state lighting.

Received 26th November 2024,
Accepted 6th January 2025

DOI: 10.1039/d4ma01163e

rsc.li/materials-advances

1. Introduction

Double tungstate compounds have garnered significant attention due to their intriguing optical and electronic properties, making them promising candidates for various technological applications.[1–4] In recent years, there has been significant interest in rare earth-based double tungstate scheelite materials due to their unique optical characteristics, such as high luminescence quantum efficiency, narrow line width and excellent thermal stability.[5–7] These materials exhibit UV absorption and emit visible light, making them well-suited for applications like phosphorescent materials, luminescent diodes and optical fibres *etc.*[8,9] Among these compounds, $ACe(WO_4)_2$ (where A = Li, Na, K) has emerged as a subject of intense research, owing to its unique defect-induced photoluminescence properties. The incorporation of alkali metal ions (Li^+, Na^+, K^+) into the crystal lattice of $ACe(WO_4)_2$ introduces defects that lead to distinct optical characteristics, opening new avenues for the design of advanced optoelectronic devices. Understanding this impact is vital for tailoring optical properties to specific applications. A recent study by Shimemura *et al.* focused on $ACe(WO_4)_2$ materials, where A represents Li^+, Na^+, and K^+. While they investigated the emission properties, detailed photoluminescence information was lacking.[10] In another report, Shimemura *et al.* discussed $LiCe(WO_4)_2$ as a fluorescent material, considering combined luminescence of Ce^{3+} and WO_4.[2–11] The photoluminescence properties of materials have gained prominence due to their applications in various fields, ranging from lighting and displays to sensors and lasers. $ACe(WO_4)_2$ compounds, with their intriguing luminescent behavior, offer a versatile platform for tailoring and optimizing photoluminescence emissions. These emissions are primarily attributed to the interaction between 4f and 5d electron orbitals of Ce^{3+} ions within

[a] *Institute of Engineering and Management (IEM), University of Engineering and Management, Kolkata, 700160, India. E-mail: nibedita.haldar@uem.edu.in; Tel: +91 8250478156*
[b] *School of Materials Science and Nanotechnology, Jadavpur University, Jadavpur, Kolkata-700032, India*

† Electronic supplementary information (ESI) available. See DOI: https://doi.org/10.1039/d4ma01163e

the crystal lattice. The manipulation of these emissions through controlled defect engineering, particularly the introduction of oxygen vacancies (V_O), provides an innovative approach to enhance the luminescence efficiency and tune the emission colors.

In this context, the present study delves into the intricate relationship between alkali metal ions, defect-induced photoluminescence, and crystal structure in $ACe(WO_4)_2$ compounds. By systematically investigating the impact of Li^+, Na^+, and K^+ ions on the defect formation and subsequent photoluminescence properties, valuable insights can be gained into the underlying mechanisms governing these phenomena. Through a combination of experimental characterization techniques and advanced theoretical modeling, a comprehensive understanding of the defect-induced photoluminescence behavior in $ACe(WO_4)_2$ compounds can be achieved. The insights garnered from this research not only contribute to the fundamental understanding of defect engineering in double tungstate materials but also pave the way for the development of novel optoelectronic devices with tailored luminescent properties.

This article presents the hydrothermal synthesis of scheelite-type $LiCe(WO_4)_2$, $NaCe(WO_4)_2$ and $KCe(WO_4)_2$ using tri-sodium citrate as an organic additive. It examines the impact of alkali metal ions on crystal structure distortion and optical properties of $ACe(WO_4)_2$ (A = Li, Na, K). As per literature, there is no report on *ab initio* band structures of $ACe(WO_4)_2$ clusters are employed to elucidate photoluminescence properties. This study provides insights into electronic and optical properties of $ACe(WO_4)_2$ and informs the development of new materials with tailored optical attributes.

2. Experimental section

2.1 Materials and synthesis

Scheelite-type $ACe(WO_4)_2$ (A = Li, Na, K) materials were synthesized using a conventional hydrothermal method. To prepare Li/Na/$KCe(WO_4)_2$, 0.17 mmol (0.074 g) of cerium nitrate [$Ce(NO_3)_3 \cdot 6H_2O$, Merck, Germany, 98.5% purity] and 0.17 mmol (0.044 g) of trisodium citrate dihydrate ($Na_3Cit \cdot 2H_2O$, Sigma Aldrich, $\geq$99.0% purity) were dissolved in 60 mL of deionized (DI) water at room temperature. Another 20 mL of an aqueous solution containing 0.34 mmol (0.089 g) of lithium tungstate ($Li_2WO_4 \cdot H_2O$, Merck, Germany, 99.0% purity) or 0.112 g of sodium tungstate ($Na_2WO_4 \cdot H_2O$, Merck, Germany, $\geq$99.0% purity) or 0.111 g of potassium tungstate ($K_2WO_4 \cdot 2H_2O$, Merck, Germany, 99.0% purity) was added dropwise over 30 minutes with continuous magnetic stirring, maintaining the pH of the reaction medium at 7. The initially transparent solution turned milky white. Subsequently, the solution was transferred into a Teflon autoclave and maintained at 180 °C for 24 hours. After cooling to room temperature, the resulting product was collected *via* centrifugation and subsequently washed with DI water and ethanol. The washed product was then dried at 70 °C for 10 hours, followed by calcination at 800 °C for 5 hours to obtain the powdered final product. Thus, materials with different alkali metal sources (Li, Na, K) were synthesized, and the resulting samples were designated as LCWO, NCWO, and KCWO respectively.

2.2 Measurement and characterization

Various analytical techniques were employed to investigate the properties of the material. X-ray diffraction (XRD) was utilized to extract structural and microstructural refinement parameters *via* the least-squares method. The Rigaku Ultima III powder diffractometer from Japan, equipped with CuK_α radiation (λ = 1.5404 Å), was employed for recording XRD patterns. The experimental profiles were fitted using the most appropriate pseudo-Voigt analytical function, accounting for asymmetry. A fourth-order polynomial function was applied to fit the background of each pattern. The sample morphology was examined using a field emission scanning electron microscope (FESEM; Hitachi S-4800) operating at 5 kV. Raman spectra were analyzed using the Alpha 300 instrument from Wintec, with a 530 nm laser (3 mW output and a 2 m spot size). Infrared spectra, ranging from 400 to 4000 cm^{-1}, were recorded using the IR Prestige. X-ray photoelectron spectra (XPS) were collected through the PHI Versa Probe III Scanning XPS Microprobe with Al K source. UV-vis absorption spectra were measured using a UV-vis spectrophotometer (V-630, JASCO). Photoluminescence emission spectra were obtained using an FP-8300, JASCO, equipped with a 100 W Xe lamp, and measurements were conducted at room temperature. The outcomes derived from these techniques hold the potential to optimize material synthesis and customize properties to suit specific applications.

2.3 *Ab initio* density functional theory

To compute the spin-polarized electronic band structure, projected density of states (PDOS), and total density of states (TDOS) for multiple atoms, the VASP simulation software was employed utilizing the plane-wave pseudopotential (PAW) method. The basis set utilized was the Perdew–Burke–Ernzerhof (PBE) exchange correlation ultra-soft potentials.[12,13] The considered atoms included Li ($1s^2\ 2s^1$), Na ($1s^2\ 2s^2\ 2p^6\ 3s^1$), K ($3s^2\ 3p^6\ 4s^1$), Ce ($5s^2\ 5p^6\ 4f^1\ 5d^1\ 6s^2$), W ($5p^6\ 6s^2\ 5d^{10}$), and O ($2s^2\ 2p^4$). The supercell structure with the lowest single-point ground state energy was optimized using a 4 × 4 × 4 Monkhorst–Pack *k*-point grid. Subsequently, the band structure was calculated along symmetry points $\Gamma \rightarrow X \rightarrow H_1 \rightarrow C \rightarrow H \rightarrow Y \rightarrow \Gamma \rightarrow C$. A plane wave cutoff energy of 520 eV was chosen, and convergence energy was achieved within the range of 220 to 620 eV. To ensure accuracy, maximum atomic displacement and stress were constrained at 5×10^{-4} Å and 0.02 GPa, respectively. Each atom was subjected to a 0.01 eV Hellmann–Feynman force. For precise computational convergence, the EDIFF and force EDIFG parameters were set to 10^{-6} eV and 10^{-3} eV, respectively. This information aids in comprehending atomic behavior within diverse materials and can guide the design of materials possessing specific electronic properties.

3. Result and discussion

3.1 Phase and crystal structure analyses of the samples by XRD, FESEM, TEM

The obtained X-ray diffraction (XRD) patterns of $ACe(WO_4)_2$ materials are presented in Fig. 1(a–c). These patterns closely resemble those of the triclinic scheelite-type material

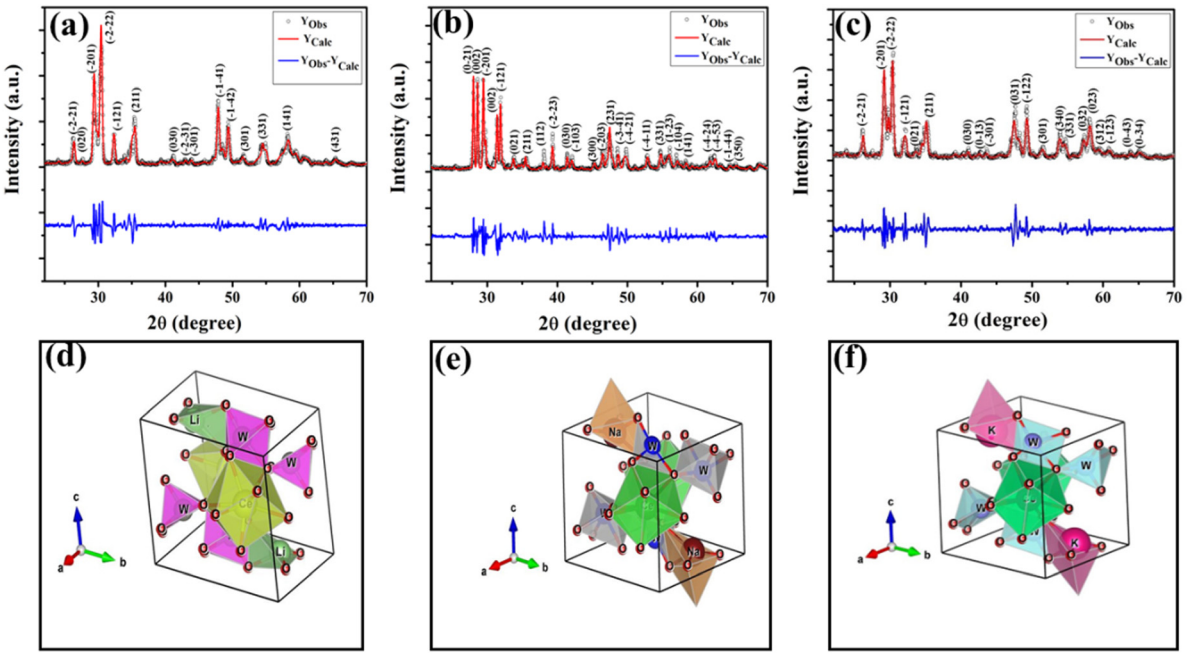

Fig. 1 XRD patterns (a)–(c) and triclinic unit cell's structure (d)–(f) of LCWO, NCWO, KCWO respectively.

(ICSD card: 200520, space group: $P\bar{1}(2)$).[14] The absence of additional peaks verifies the phase purity of the samples and a strong agreement between observed and calculated XRD patterns *via* Rietveld refinement is evident. The refinement process was pursued until R_p, R_{wp}, R_{exp}, and χ^2 converged within acceptable ranges.[15] Detailed structural refinement information is available in Tables S1 and S2 of the ESI.† The refinement reveals that W, Ce, and A atoms form a cage-like structure connected by O atoms. Ce atoms establish regular CeO_8 polyhedra, A atoms form AO_4 tetrahedra, and W atoms create WO_6 octahedra with 8, 4, and 6 coordinated O atoms, respectively. Each AO_4 shares an edge with WO_6 octahedra and links to CeO_8 polyhedra through O atoms. Schematic representations of the triclinic unit cell of ACWO are depicted in Fig. 1(d)–(f). Rietveld analyses additionally indicate that W atoms possess inversion symmetry, resulting in edge-sharing octahedra forming W_4O_{16} as a tetramer *via* W_2O_2 bridged O atoms. The lattice parameters, unit cell volume, A–O, Ce–O, and W–O bond lengths, as well as A–O–W, Ce–O–W, and O–Ce–O bond angles, decrease in LCWO and KCWO compared to NCWO unit cells, indicating distortion of the unit cells. This trend can be attributed to the ionic radius of Na^+ (r = 0.99 Å, CN = 4), which is closest to that of Ce^{3+} (r = 1.14 Å, CN = 8), compared to the ionic radius of Li^+ (r = 0.59 Å, CN = 4) and K^+ (r = 1.37 Å, CN = 4). As a result, the crystal compactness is most significant in NCWO while both LCWO and KCWO show abnormal lattice distortion. The lower lattice parameters observed in LCWO and KCWO compared to NCWO can be attributed to the distinct ionic sizes and coordination number mismatches resulting from the substitution of Ce^{3+} with Li^+ and K^+.[16,17] The significantly smaller ionic radius of Li^+ induces a compression of the lattice as it attempts to accommodate the smaller ions, leading to reduced lattice parameters in LCWO. Conversely, the larger ionic radius of K^+ results in lattice distortion due to spacing mismatches, contributing to a decrease in lattice parameters in KCWO. These combined effects, arising from differences in ionic radii and coordination numbers, lead to lattice distortions and a subsequent decrease in lattice parameters in both LCWO and KCWO compared to NCWO.

The degree of CeO_8 polyhedron distortion (K) is quantified as ~1.066, 1.046, and 1.082 for LCWO, NCWO, and KCWO using the relation $K = \frac{d_1(\mathrm{Ce-O})}{d_2(\mathrm{Ce-O})}$, where d_1(Ce–O) and d_2(Ce–O) represent different bond lengths. Similarly, WO_6 octahedron distortion (N) is assessed as ~1.132, 1.095, and 1.285 using the relation $N = \frac{\alpha_1(\mathrm{O-W-O})}{\alpha_2(\mathrm{O-W-O})}$, where α_1(O–W–O) and α_2(O–W–O) denote distinct bond angles, affirming greater V_O-induced distortion in LCWO and KCWO compared to NCWO.[18] Furthermore, a reduction in the c/a ratio in NCWO relative to LCWO and KCWO indicates the influence of dipole–dipole interactions on short-range disorder attributed to charge entrapment at the V_O site.[19]

The field emission scanning electron microscopy (FESEM) analysis demonstrates notable morphological variations among the ACWO samples, depicted in Fig. 2(a–c). LCWO exhibits an irregular shape, whereas a truncated octahedral morphology is observed in NCWO and KCWO. This structure becomes more pronounced in NCWO, attributed to enhanced crystal compactness. These findings highlight the pivotal role of alkali metal ions in modulating the morphology during the hydrothermal synthesis process. To gain more insights into the precise shape and size of the particles, further analysis was conducted using transmission electron microscopy (TEM). Upon TEM examination, the samples

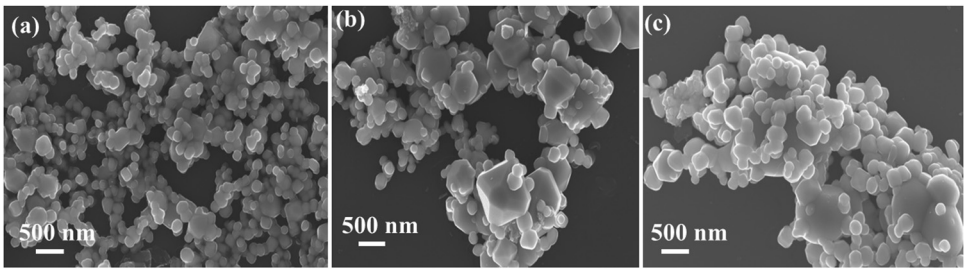

Fig. 2 (a)–(c) FESEM image of LCWO, NCWO, KCWO respectively.

exhibited irregular to truncated octahedral shapes and sizes (Fig. 3(a), (d) and (g)) for LCWO, NCWO, and KCWO, respectively. High-resolution TEM (HRTEM) images allowed for the determination of *d*-spacing values, which were found to be 0.176 nm for LCWO, 0.142 nm for NCWO, and 0.263 nm for KCWO (Fig. 3(b), (e), and (h)). These *d*-spacing values correspond to the (301), (350), and (021) planes of LCWO, NCWO, and KCWO, respectively. Notably, these results are consistent with the X-ray diffraction (XRD) data presented in Fig. 1(a–c). Fig. 3(c), (f), and (i) illustrate the selected area electron diffraction (SAED) patterns of LCWO, NCWO, and KCWO samples, respectively, derived from the TEM images. The diffraction spots represented by white points in these patterns correspond to specific crystal planes. Importantly, these diffraction spots (Fig. 3(c), (f) and (i)) align well with the XRD data shown in Fig. 1(a–c). The HRTEM images along with their corresponding *d*-spacing measurements support the crystallographic properties of LCWO, NCWO, and KCWO samples. These observations validate the structural characteristics of the materials under investigation.

3.2 Investigations of defects in ACWO nanostructures by FTIR, Raman and X-ray photoelectron spectroscopies

FTIR and Raman spectra serve as analytical techniques to assess structural distortions in terms of vibrational frequencies. In the context of materials like ACWO, these techniques offer insights into crystal structure and the presence of defects, such as vacancies (V_O). The FTIR spectrum of ACWO manifests four absorption bands (Fig. S1, ESI†), corresponding to internal vibrations of the WO_6 octahedron. Within the W^RO_6 structure, tungsten ions occupy the centre of regular octahedra formed by six oxygen ions with 2i site symmetry. Group theory dictates that the symmetry modes can be expressed as Γ_{Oh}= 36 A_u.

The emergence of an oxygen vacancy within the lattice can lead to a distorted octahedral structure, specifically the W^DO_6

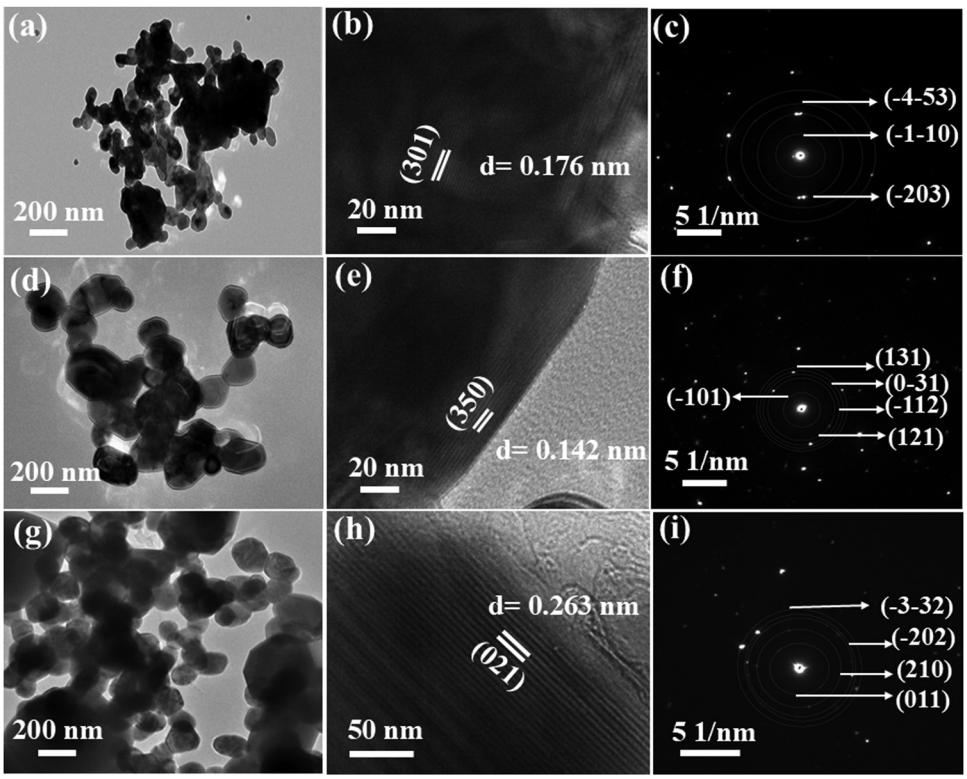

Fig. 3 TEM image, HRTEM image and corresponding SAED pattern of LCWO (a)–(c), NCWO (d)–(f), KCWO (g)–(i) respectively.

octahedron. This introduces a reduction in lattice symmetry, subsequently affecting the vibrational frequencies of the system. The detailed deconvolution of FTIR bands is provided in the ESI† (Table S3). Deconvolution of two bands (780–920 and 673–715 cm^{-1}) in the FTIR spectra reveals the peaks at 679, 693, 697, 797, 823, 868 cm^{-1} for NCWO. Peaks at 697 and 868 cm^{-1} correspond to the stretching vibration ($\rightarrow O \rightarrow W \rightarrow O \rightarrow$) of W^DO_6 and W^RO_6 octahedra respectively. Other deconvoluted peaks align with the asymmetric stretching of two-oxygen bridged W_2O_2 in W^RO_6 and W^DO_6 octahedra.[20,21] This blue shift in the FTIR spectrum of LCWO and KCWO signifies defects introduced into the crystal lattice, leading to alterations in the local chemical environment of atoms or molecules within the material. The peaks at 733 and 748 cm^{-1} for NCWO, correspond to W–O bending vibration of W^DO_6 and W^RO_6 respectively (Fig. 4). Similarly, a blue shift is also observed for LCWO and KCWO.[22,23] However, that peak shifting alone may not be sufficient to fully characterize a material's defects. Weighted percentage calculation from area under the curves indicates W^DO_6 ~44%, 30%, and 48% for LCWO, NCWO, and KCWO respectively. A noticeable blue shift is observed in LCWO and KCWO, indicating more pronounced V_O in those samples than in NCWO. The W^DO_6/W^RO_6 ratios stand at 0.785, 0.428, and 0.923 for LCWO, NCWO, and KCWO respectively, indicating greater octahedral distortion in LCWO and KCWO compared to NCWO.

The Raman spectrum of NCWO exhibits peaks at 338, 389, 463, and 534 cm^{-1}, aligning with the vibrational motion of WO_6 octahedra and W_2O_2 units (Fig. 5). The peak at 463 cm^{-1} is attributed to the A_g symmetric stretching mode of the W_2O_2 unit. The remaining peaks correspond to asymmetric and symmetric bending vibrations of O–W–O within the A_g mode, along with the asymmetric stretching mode of the W_2O_2 unit.[24,25] Furthermore, the relatively lower intensity of Raman peaks observed in KCWO and LCWO compared to NCWO can be attributed to symmetry disruption caused by an increased presence of oxygen vacancies and antisite defects.[26] The other peaks at 680, 786, 930 cm^{-1} are due to secondary scattering.

XPS analysis was undertaken to delve into the chemical states of Li, Na, K, Ce, W, and O, aiming to enhance comprehension of V_O-induced disorder effects on material electronic structure. The obtained XPS data for all elements were adjusted to account for the C 1s peak attributed to adventitious carbon on the sample surface due to atmospheric exposure.[27] This C 1s

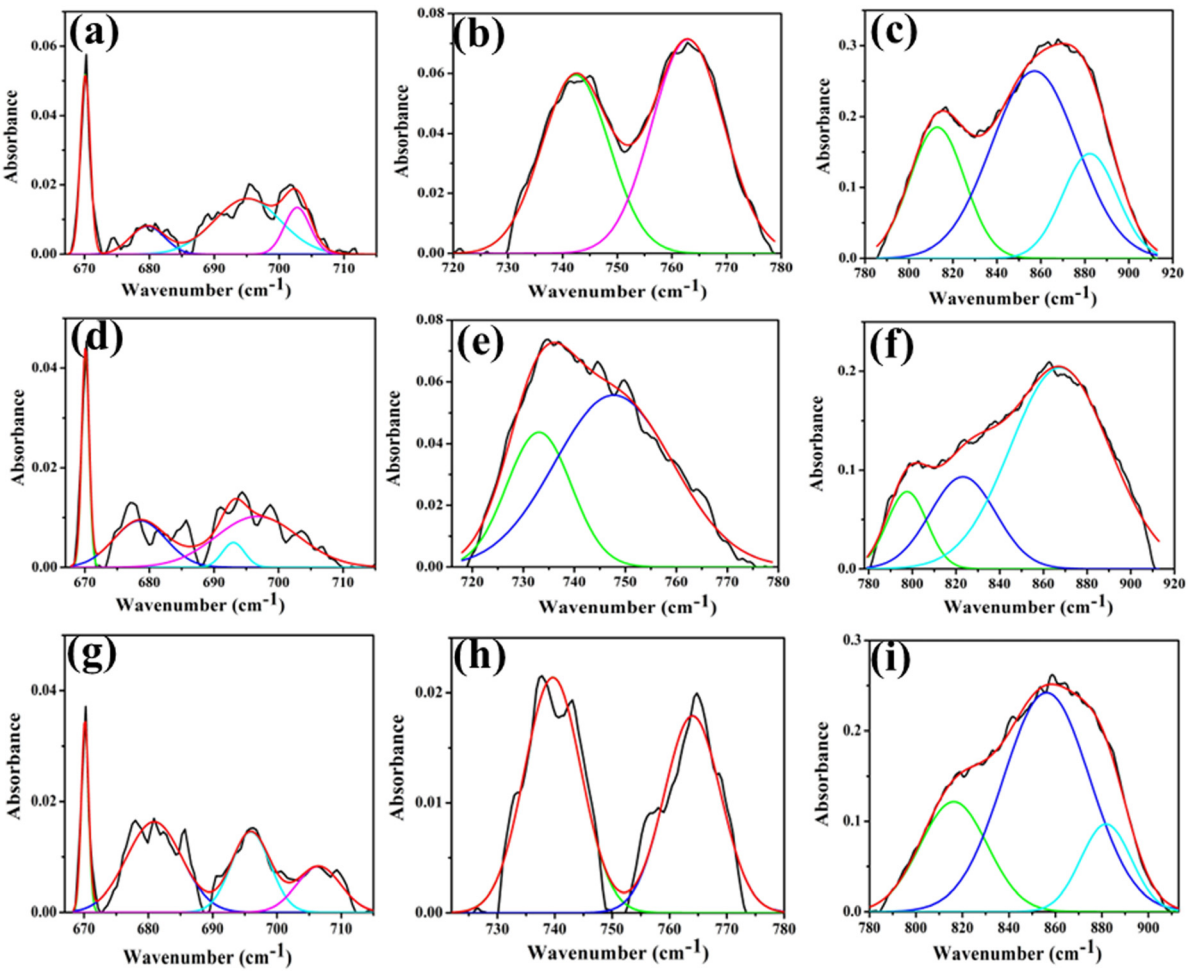

Fig. 4 (a) Deconvoluted curves of the FTIR bands 660–717, 718–777 and 778–910 cm^{-1} of LCWO (a)–(c), NCWO (d)–(f) and KCWO (g)–(i) respectively.

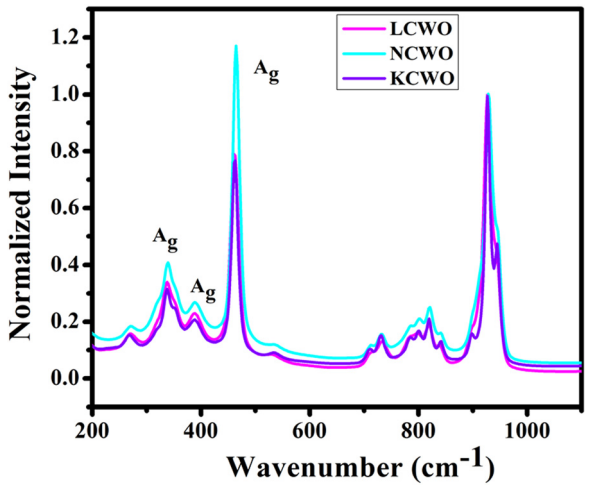

Fig. 5 Raman spectra of ACWO nanostructures.

peak carries a binding energy of 284.6 eV. The survey scan (Fig. S2 of ESI†) encompasses core binding energies of Li, Na, K, Ce, W, and O within the energy range of 0 to 1100 eV. This scan aids in identifying chemical states present in the samples. Further, high-resolution spectra of W, Ce, and O from all samples are illustrated in Fig. 6. These spectra offer detailed insights into the electronic structure of these materials, particularly highlighting changes prompted by the presence of V_O-induced disorder.

Fig. 6(a)–(c) reveal two asymmetric peaks in XPS spectra at 35.4 and 37.4 eV, originating from spin–orbit splitted $4f_{7/2}$ and $4f_{5/2}$ orbitals of W^{6+}.[28–30] Deconvolution of these spectra results in four peaks, W_a, W_b, W_c, and W_d, corresponding to diverse electronic states of W. W_a and W_c associate with W^DO_6, while W_b and W_d signify W^RO_6. The electronegativity disparity between W and O suggests an ionic W–O bond. The presence of V_O heightens the effective charge on W, inducing electron–electron repulsion and reducing binding energies of the $4f_{7/2}$ and $4f_{5/2}$ states in W^DO_6. Estimated W^DO_6 percentages are higher in LCWO (~43%) and KCWO (~45%) compared to NCWO (~26%), aligning with FTIR findings. In Fig. 6(d)–(f), two asymmetric peaks within the ranges 877–891 eV and 895–910 eV manifest in Ce 3d spectra. Deconvolution of the $3d_{5/2}$ peak yields three peaks, Ce_a, Ce_b, and Ce_c, associated with distinct Ce electronic environments. Ce_c corresponds to CeO_8, while Ce_a and Ce_b relate to CeO_7 and CeO_6, containing V_O and $2V_O$, respectively. Analysis of Ce spectra demonstrates V_O's impact, shortening Ce–O bond lengths and heightening

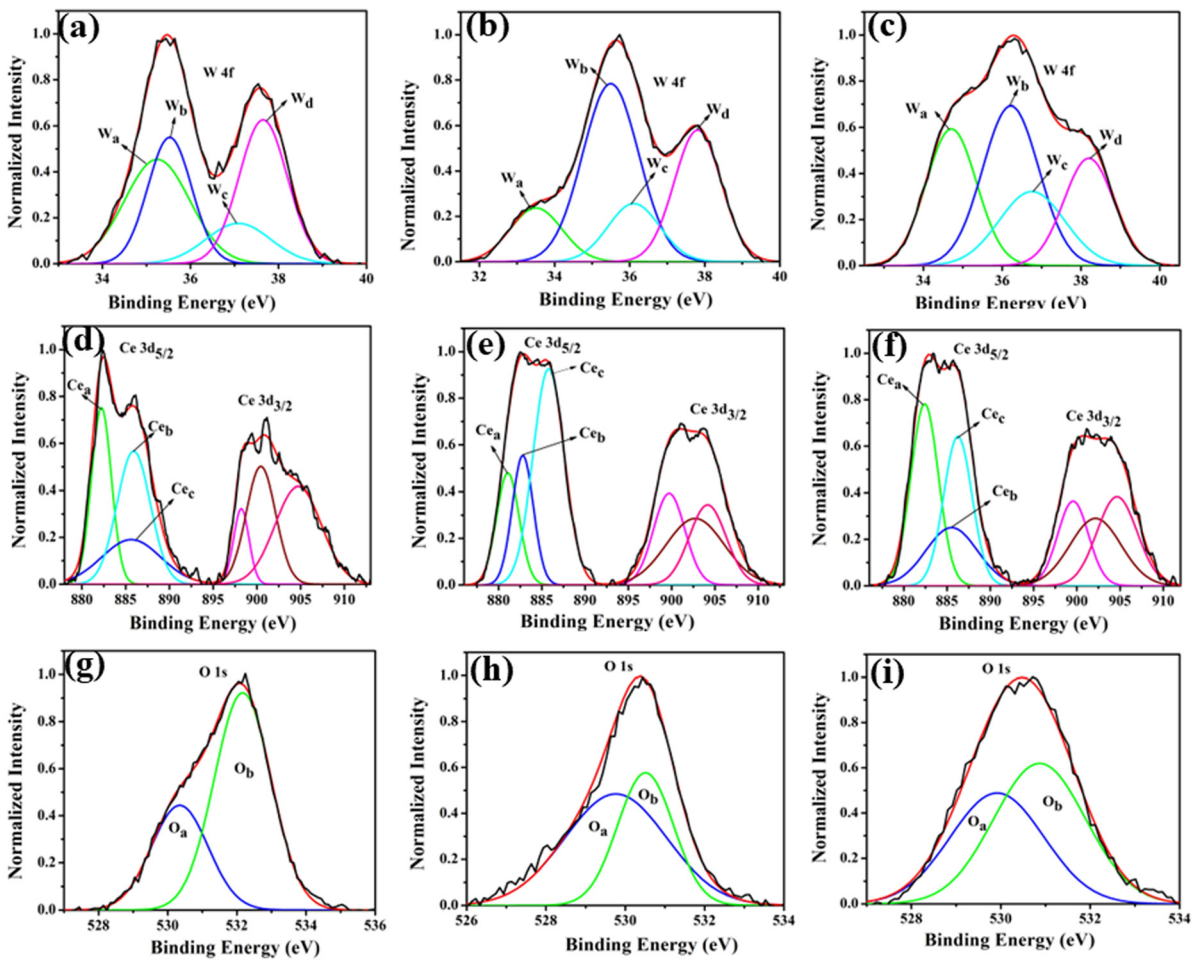

Fig. 6 (a)–(c) XPS W 4f, (d)–(f) XPS Ce 3d, (g)–(i) XPS O 1s core level spectra of LCWO, NCWO, KCWO respectively.

electron–electron repulsion at the Ce site, thereby lowering binding energies of $3d_{5/2}$ and $3d_{3/2}$ orbitals.[31] Scrutinizing the data indicates a reduction in Ce_a weight percentage in NCWO (~21%) compared to LCWO (~34%) and KCWO (~40%), implying V_O suppression in NCWO. XPS analysis of O 1s manifests an asymmetric peak. Deconvolution of this spectrum yields one peak at 530.6 eV, attributed to lattice oxygen within Ce–O–Ce bonds in the crystal structure.[32–34] Another peak at 532.4 eV corresponds to chemisorbed oxygen linked to oxygen vacancies. Notably, the area under the peak at 532.4 eV is greater in LCWO and KCWO compared to NCWO, signifying a higher oxygen vacancy amount in those samples than in NCWO.

3.3 Optical properties of the as-prepared ACWO samples by UV-vis, photoluminescence spectroscopy

The UV-vis absorption spectra of ACWO materials reveal an optical band gap of approximately 3.10 eV for LCWO, 3.14 eV for NCWO, and 3.06 eV for KCWO (depicted in Fig. S3, ESI†). The valence band (VB) of ACWO consists of O 2p–W 5d hybridization, while the conduction band (CB) of ACWO comprises W-5d, Ce-4f, and a minor contribution of O-2p, as indicated by a DFT-based *ab initio* calculation (discussed later).[35] A broad peak at 380 nm is observed in the photoluminescence excitation (PLE) spectra for ACWO samples when monitored at an emission wavelength of 531 nm (Fig. S4, ESI†). The 380 nm peak in the PLE spectra is attributed to charge transfer (CT) absorption within WO_6 octahedra. This absorption process involves electronic charge transfer between different atomic species, specifically between O-2p and W-5d within the WO_6 octahedra. Furthermore, the emission spectra recorded in the visible region with an excitation wavelength of 380 nm are illustrated in Fig. 7(a)–(c). The emission spectra in the visible region upon excitation at 380 nm likely correspond to the relaxation of excited states formed during the CT absorption process. The luminescence characteristics of the samples reveal four peaks in the visible region upon excitation at 380 nm. A prominent peak is observed at 439 nm (blue I, 22 779 cm^{-1}), followed by two peaks in the blue region at 462 nm (blue II, 21 645 cm^{-1}) and 487 nm (blue III, 20 533 cm^{-1}), along with a green emission at 531 nm (green, 18 832 cm^{-1}). Previous studies have proposed that emissions from scheelite materials are largely due to 5d to 4f transitions within rare earth elements. However, the precise mechanism remains debated due to factors such as crystal field, polarizability, *etc.*, significantly affecting emission characteristics.[36]

To comprehend the emission wavelength (λ) based on the 5d–4f transition of Ce^{3+} within a regular CeO_8 polyhedron, we have employed a relationship provided by van Uitert *et al.*:[37]

$$\frac{1}{\lambda} = \frac{Q^*}{hc}\left[1 - \left(\frac{V}{4}\right)^{\frac{1}{V}} 10^{\frac{-(nrE_a)}{80}}\right] \quad (1)$$

where, Q^* represents the energy of 5d band edge of free Ce^{3+} ion (= 50 000 cm^{-1}), V is the valence of the Ce^{3+}, '*n*' is the number of anions in the immediate shell around Ce^{3+}, E_a is electron affinity of the atoms forming anions and '*r*' is defined as the difference between average bond length and radius of anion of CeO_8 polyhedra (1.03 Å). We have calculated wavelength ~437 nm is highly corroborating with our experimental blue I emission at 439 nm. By using eqn (1) with CeO_7 and CeO_6 configurations, it was calculated that the emission wavelengths for these configurations are approximately 470 nm and 522 nm, respectively. These values match well with the experimentally observed blue III and green emissions (as shown in Fig. 7). It is believed that V_O defects alter the energy of the 5d orbitals of Ce^{3+} in CeO_7 and CeO_6, resulting in different emissions. To further understand this, the crystal field stabilization energy and centroid shift of the d-orbitals (ε_c(1, 3+, A)) of Ce^{3+} in different CeO_8 polyhedra were calculated using Dorenbos's eqn (2) and (3):[38]

$$\varepsilon_{cfs}(1, 3+, A) = \beta R_{av}^{-2} \quad (2)$$

$$\varepsilon_c(1, 3+, A) = 6.35 - E^C(1, 3+, A)\ \text{eV} \quad (3)$$

where, β = 1.35 × 109 pm^2 cm^{-1} for Ce^{3+} and $R_{av} = \frac{1}{N}\sum_{i=1}^{N}(R_i - 0.6\Delta R)$; R_i denotes bond lengths to the N coordinating anions in distorted lattice.

The calculated values of $\varepsilon_c(1, 3+, Ce^{3+})$ for CeO_8, CeO_7, and CeO_6 are approximately 5.94, 5.66, and 5.41 eV for LCWO, 5.93, 5.69, and 5.46 eV for NCWO, and 5.92, 5.62, and 5.35 eV for KCWO, respectively. Furthermore, the values of $\varepsilon_{cfs}(1, 3+, Ce^{3+})$ are in the order of 2.06, 3.44, and 4.69 eV for LCWO, 2.01, 3.30, and 4.42 eV for NCWO, and 2.16, 3.62, and 4.99 eV for KCWO, respectively. It was also determined that the difference between the $^5D_0$–$^2F_{5/2}$ and $^5D_0$–$^2F_{7/2}$ transitions is sapproximately 2000 cm^{-1}. The emissions labelled as "blue I" and "blue II" exhibit a distinct energy difference of around 1134 cm^{-1}. This disparity suggests that these emissions have different energy levels, indicating that the "blue II" emission cannot be attributed to the $^5D_0$–$^2F_{7/2}$ transition within CeO_8 polyhedra or a 5d orbital split transition. This implies that the origin of the "blue II" emission differs from these known transitions. The presence of two distinct $\varepsilon_c(1, 3+, Ce^{3+})$ states within CeO_6 units are associated with the existence of two vacancy oxygen (V_O) defects (discussed later in DFT calculation). An intriguing finding is that the centroid shift $\varepsilon_c(1, 3+, Ce^{3+})$ value of CeO_7 and CeO_6 is observed to decrease, indicating presence of more oxygen vacancies in KCWO and LCWO compared to NCWO. This suggests that V_O defects significantly influence the values of ε_{cfs} and ε_c, consequently determining the emission wavelength (λ) for the 5d–4f transition within CeO_7 and CeO_6.

The formation of V_O and $2V_O$ defects can be comprehended through the Kröger–Vink notation, which delineates the relationship between defects and stoichiometry in ionic crystals. Electrons are released into the host matrix, leading to the creation of ionized defect states $V_O^{\bullet}$ and $2V_O^{\bullet}$ which can be represented by eqn 4(a) and 4(b):

$$[CeO_8]^{\times} + [CeO_7\text{-}V_O^{\times}] \rightarrow [CeO_8]' + [CeO_7\text{-}V_O^{\bullet}] \quad (4a)$$

$$[CeO_8]^{\times} + [CeO_6\text{-}2V_O^{\times}] \rightarrow [CeO_8]'' + [CeO_6\text{-}2V_O^{\bullet}] \quad (4b)$$

where $[CeO_8]'$ and $[CeO_8]''$ denote electron donors and $[CeO_7\text{-}V_O^{\bullet}]$ and $[CeO_6\text{-}2V_O^{\bullet}]$ are the electron acceptors those exhibit blue III and green emission.

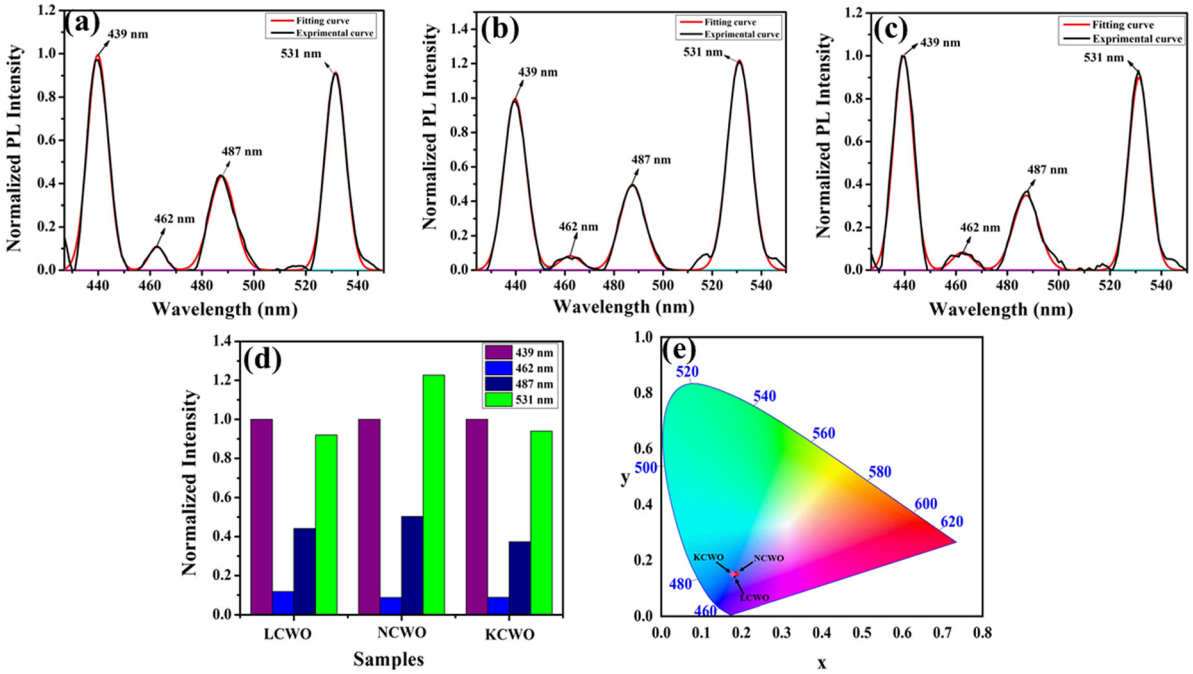

Fig. 7 Photoluminescence spectra of (a) LCWO, (b) NCWO and (c) KCWO respectively. (d) Normalized PL intensity ratio of emission wavelengths (e) The CIE chromaticity diagram of the ACWO.

Additionally, the luminescent intensity demonstrates variations with the presence of Li^+, Na^+, and K^+ ions. Specifically, NCWO exhibits the strongest intensity for blue III and green emissions, whereas LCWO and KCWO display relatively weaker intensity for these emissions. It is suggested that the presence of A^+ ions affects the lattice parameters, thereby influencing the crystal field that surrounds the rare earth ions.[39] In our study, it is evident that the alkali metal ions do not alter the shape and peak position of the photoluminescence (PL) spectra; rather, they solely affect the luminescence intensity. It has been previously confirmed that NCWO exhibits reduced lattice distortion compared to LCWO and KCWO. This reduction in lattice distortion is associated with an increase in luminescence intensity in NCWO compared to both LCWO and KCWO.[40,41] We have also checked the stability of the materials in terms of fluorescent spectra taken over a duration of 7 days, one month, and two months (Fig. S5, ESI†). The estimated Commission Internationale de l'Eclairage (CIE) coordinates are (0.179, 0.148), (0.181, 0.149), and (0.178, 0.148) for LCWO, NCWO, and KCWO, respectively, indicating a blue emission (Fig. 7(e)).[42,43] However, the variations in the coordinates are attributed to different contributions from blue II and III emissions. According to eqn (5), the color purity is calculated to be approximately 91% for all samples.

$$\text{Color purity} = \frac{\sqrt{(x-x_i)^2+(y-y_i)^2}}{\sqrt{(x_d-x_i)^2+(y_d-y_i)^2}} \times 100\% \qquad (5)$$

where (x, y) represents the color coordinates of the phosphor; (x_i, y_i) is the illuminant point of the 1931 CIE Standard Source with the colour coordinates of (0.3101, 0.3162); (x_d, y_d) refers to colour coordinates of the dominant wavelength and the correlated colour temperatures (CCTs) have been calculated from McCamy's relation as given in eqn (6),[44] and it was found that (CCTs) ~ 7763, 7803 and 7784 K for LCWO, NCWO and KCWO respectively.

$$\text{CCT} = 449n^3 + 3525n^2 + 6823.3n + 5520.3 \qquad (6)$$

where $n = \frac{(x-0.3320)}{(0.1858-y)}$ and (x, y) represents the chromaticity co-ordinates. Hence, it may be stated that ACWO materials are excellent for blue lightening.

3.4 Density functional theory (DFT) calculation of ACWO

In our study, *ab initio* density functional theory was employed to investigate the electronic properties and optical emissions induced by vacancies (V_O, $2V_O$) in ACWO materials. We performed calculations on the electronic band structure, total density of states (TDOS), and angular momentum projected partial densities of states (PDOS) for both pure ACWO and structurally distorted ACWO models containing V_O and $2V_O$. These models were created by removing oxygen atoms to mimic the CeO_7 (V_O) and CeO_6 ($2V_O$) structures. Through optimization of the ACWO unit cell, we determined lattice parameters and bond lengths consistent with experimental results, providing confidence in the accuracy of our calculations. To begin, we set the top of the valence band maxima (VBM) to zero in all calculations. ACWO exhibited behavior as an indirect band material, with energy gaps (E_g) approximately 3.19 eV, 3.14 eV, and 3.15 eV for LCWO, NCWO, and KCWO, respectively, at the Γ- and X-points (depicted in Fig. 8(a), 9(a), and 10(a)). While the conduction band minimum (CBM) showed spin polarization, the valence band maximum (VBM) remained spin-unpolarized. These calculated band gap values closely matched experimental values, attesting to the accuracy of our calculations (as illustrated

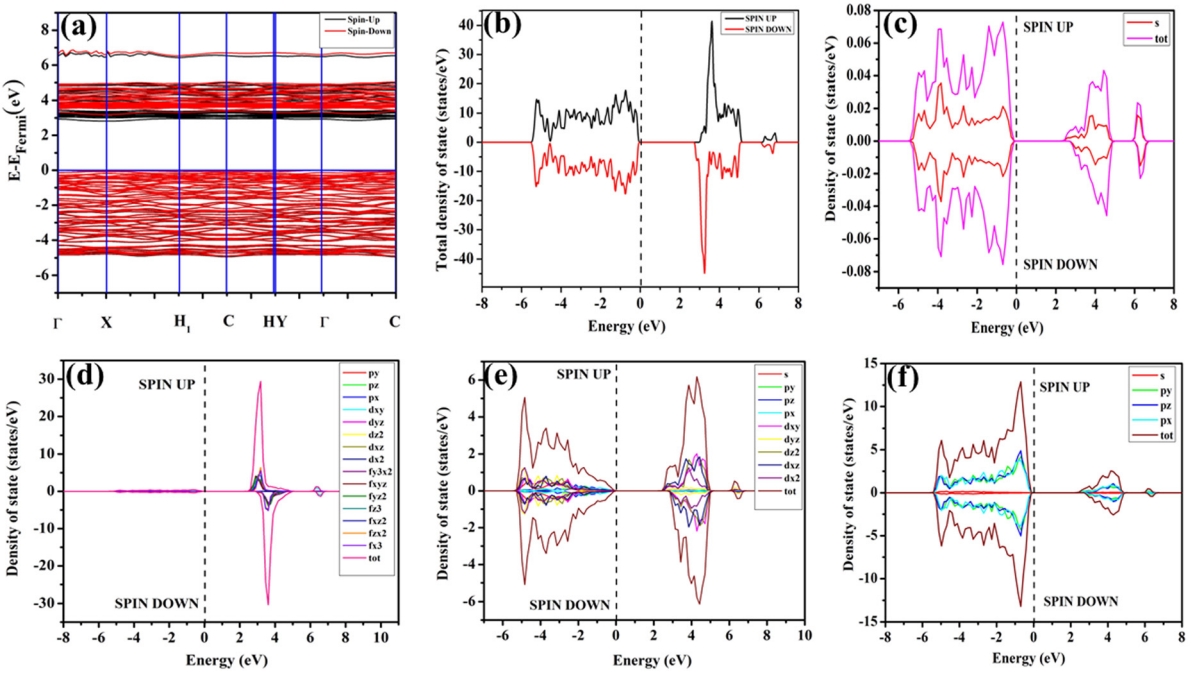

Fig. 8 (a) Band structure and (b) spin polarised TDOS and PDOS of (c) Li, (d) Ce, (e) W and (f) O of pristine-LCWO.

in Fig. S3, ESI†). The pronounced curvature at CBM implied a low effective electron mass, suggesting high electron mobility within ACWO and a longer mean free path for electrons. Conversely, the curvature at VBM was comparatively low, indicating a higher effective hole mass.

By analyzing the PDOS of A, Ce, W, and O atoms (depicted in Fig. 8(b–f), 9(b–f), and 10(b–f)), we determined that the upper portion of the valence band is predominantly influenced by O-2p_x, 2p_y, and 2p_z orbitals, with additional contributions from W-2p_x, 2p_y, and 2p_z orbitals, resulting in minimal curvature. The lower part of the valence band was primarily hybridized with W-5d_{xz}, 5d_{xy}, 5d_{yz}, 5d_{z^2}, and O-2p_x, 2p_y, and 2p_z orbitals. Contributions from Li-2s, Na-3s, K-4s, and Ce-4f orbitals were absent in ACWO samples for valence band formation. Within the CBM, spin-up Ce-4f_{z^3}, 4f_{zx^2}, 4f_{xz^2}, and 4f_{x^3} orbitals were dominant in LCWO, while spin-down Ce-4f_{z^3}, 4f_{zx^2}, 4f_{xz^2}, and

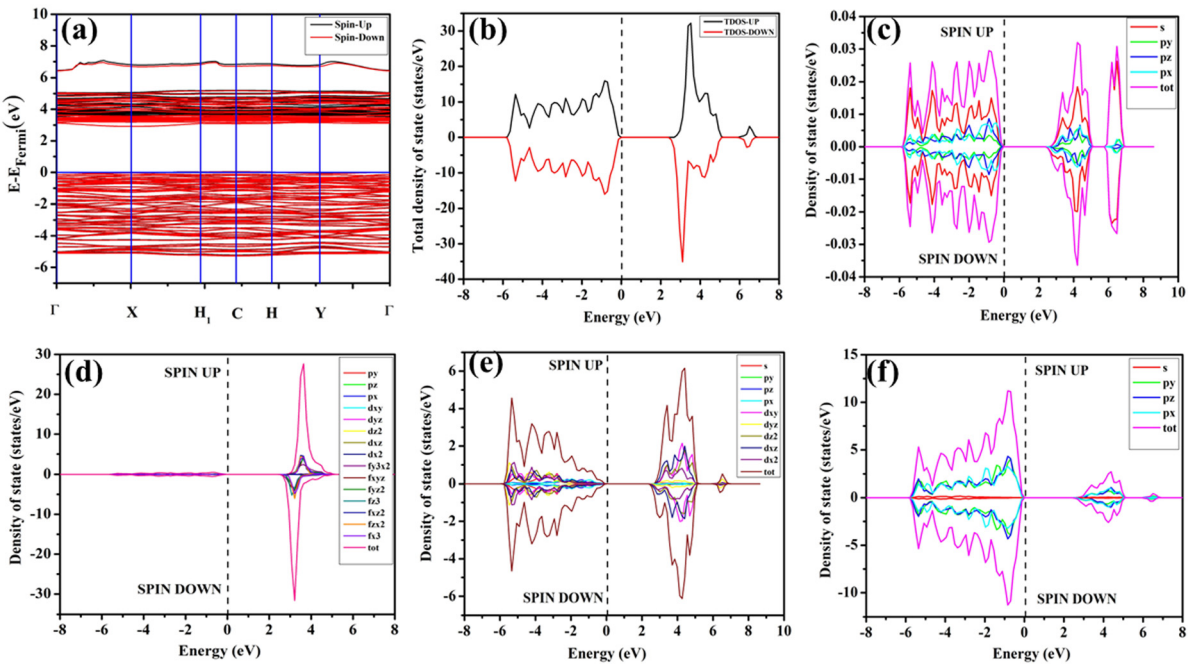

Fig. 9 (a) Band structure and (b) spin polarised TDOS and PDOS of (c) Na, (d) Ce, (e) W and (f) O of pristine-NCWO.

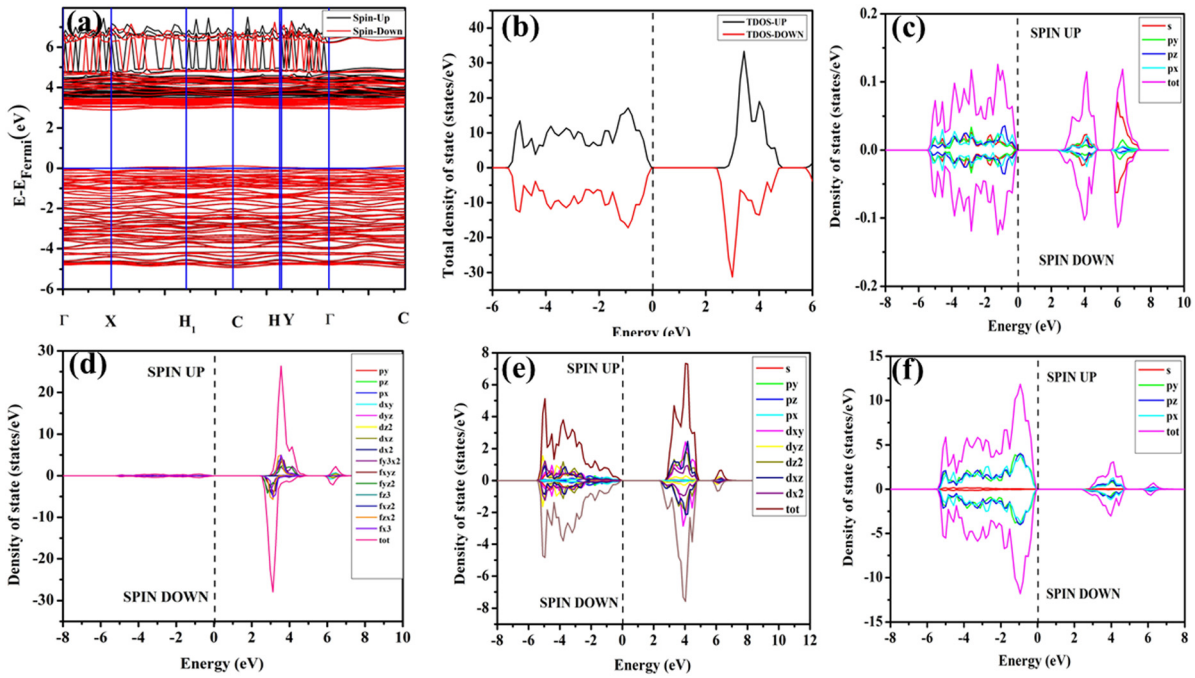

Fig. 10 (a) Band structure and (b) spin polarised TDOS and PDOS of (c) K, (d) Ce, (e) W and (f) O of pristine-KCWO.

$4f_{x^3}$ orbitals were prevalent in NCWO and KCWO samples. These orbitals were hybridized with O-$2p_x$, $2p_y$, and $2p_z$ orbitals, resulting in heightened curvature within the conduction band. The upper layer of the CB was composed of W-$4d_{xy}$, $4d_{xz}$, and $4d_{z^2}$ orbitals. Based on our findings, we concluded that the valence band is mainly constructed by WO_6 octahedra, while both CeO_8 polyhedra and WO_6 octahedra contribute to the conduction band in ACWO materials. This insight led us to affirm that the band-to-band optical transitions occur through a Ce ↔ O charge transfer process.

The band structures, total densities of states (TDOS), and angular momentum projected partial densities of states (PDOS) for ACWO samples induced by $V_O^{\bullet}$ and $2V_O^{\bullet}$, denoted as ACWO-$V_O^{\bullet}$ and ACWO-$2V_O^{\bullet}$, have been depicted in Fig. (S6–S8, ESI†) and Fig. (S9–S11, ESI†), respectively. In these figures, it is evident that the valence band maximum (VBM) of ACWO-$V_O^{\bullet}$ remains unaltered at the Γ-point, while that of ACWO-$2V_O^{\bullet}$ shifts to the X-point. Similarly, the conduction band minimum (CBM) remains constant at the Γ-point for ACWO-$V_O^{\bullet}$, whereas it shifts along the Γ–X line for ACWO-$2V_O^{\bullet}$. The calculated energy gaps (E_g) for ACWO with $V_O^{\bullet}$ and $2V_O^{\bullet}$ are (2.95 and 2.87), (2.99 and 2.97), and (3.00 and 2.96) eV for LCWO, NCWO, and KCWO, respectively. These results are presented in Fig. S6(a), S7(a), and S8(a) (ESI†). The TDOS (Fig. S6(b), S7(b), S8(b), S9(b), S10(b),

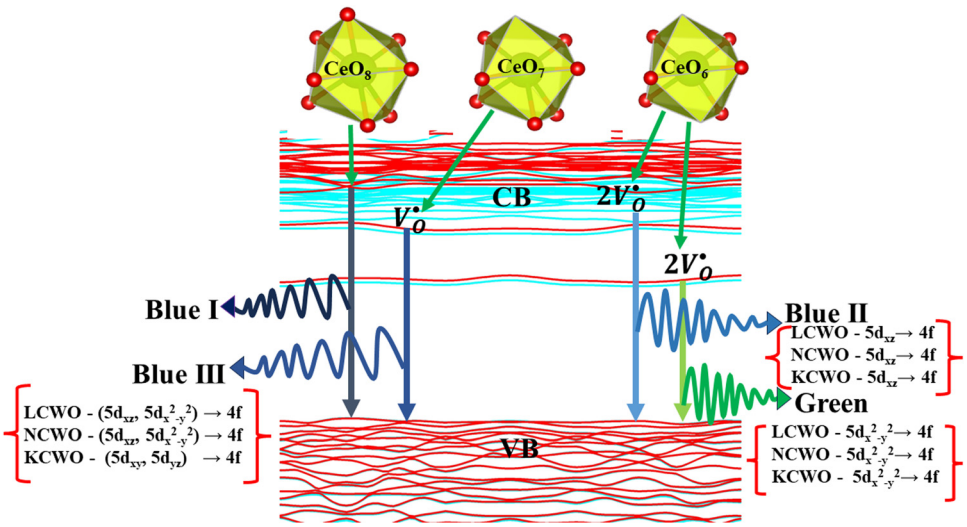

Fig. 11 Schematic representation of photoluminescence transitions of ACWO nanomaterial involving different orbitals.

and S11(b), ESI†) and PDOS (Fig. S6(c)–(f), S7(c)–(f), S8(c)–(f), S9(c)–(f), S10(c)–(f), and S11(c)–(f), ESI†) calculations revealed that the valence bandwidth decreased in ACWO-2$V_O^{\bullet}$ due to increased localization of O-2p orbitals. This led to an enhanced curvature in both ACWO-$V_O^{\bullet}$ and ACWO-2$V_O^{\bullet}$. This behaviour was attributed to an increased overlap between Ce-4f_{z^3}, 4f_{zx^2}, 4f_{xz^2}, 4f_{x^3} and O-2p_x, 2p_y, 2p_z orbitals, resulting from a reduction in Ce–O bond lengths within CeO_8 polyhedra. These modifications have the potential to influence carrier mobility through oxygen vacancies.

Further analysis indicated that LCWO-2$V_O^{\bullet}$ exhibited energy gaps of (2.10, 2.81) eV above VBM, NCWO-2$V_O^{\bullet}$ displayed energy gaps of (2.14, 2.92) eV above VBM, and KCWO-2$V_O^{\bullet}$ demonstrated energy gaps of (2.21, 2.94) eV above VBM. In contrast, LCWO-$V_O^{\bullet}$ exhibited a defect state at 2.45 eV, NCWO-$V_O^{\bullet}$ at 2.31 eV, and KCWO-$V_O^{\bullet}$ at 2.38 eV above VBM. Through a meticulous examination of TDOS and PDOS, it was deduced that the Ce-5d_{xz}, 5$d_{x^2-y^2}$, 5d_{xy}, and 5d_{yz} orbitals played a pivotal role in the emission properties of ACWO samples containing $V_O^{\bullet}$ and 2$V_O^{\bullet}$. A comprehensive list of the orbitals involved in different emissions stemming from diverse deformed structures of CeO_8 polyhedra is provided in Table S5 (ESI†) and schematically represented in Fig. 11.

4. Conclusions

Pristine ACWO (A = Li, Na, K) clusters were synthesized using a trisodium citrate-assisted hydrothermal method. Notably, as per literature, there is no report on the synthesis procedure for LCWO and KCWO *via* hydrothermal methods, along with the characterization of their emission properties. These properties reveal pronounced blue I and green emissions, alongside relatively weaker blue II and blue III emissions. Through comprehensive experimental and theoretical investigations, we have demonstrated that all these transitions, occurring within distinct configurations of CeO_8 polyhedra, are linked to the Ce 5d → 4f transition. In particular, CeO_8 and CeO_7 configurations exhibit blue I and blue III emissions, while the CeO_6 configuration emits blue II and green colors. This observation suggests that ACWO holds promise as a material suitable for blue light-emitting diodes (LEDs). Our calculations underscore the sensitivity of the O-2p and O-2p–Ce-5d orbitals, which constitute the valence and conduction bands, to defect states. These characteristics can be exploited to finely tune the electrical properties of ACWO. In essence, this research contributes to a deeper comprehension of the optoelectronic traits of pristine $ACe(WO_4)_2$ and its oxygen vacancy content. This understanding has implications for the potential applications of $ACe(WO_4)_2$, particularly in the domain of optoelectronic devices such as LEDs.

Data availability

All the data will be available on request.

Conflicts of interest

There are no conflicts to declare.

Acknowledgements

One of the authors (NH) thanks Institute of Engineering and Management (IEM), University of Engineering and Management Kolkata, 700160, India, (TM) thanks CSIR, Govt. of India, for financial support during execution of their work. NH and TM have equal contribution to this manuscript.

References

1 V. V. Atuchin, V. G. Kesler, N. Y. Maklakova, L. D. Pokrovsky and D. V. Sheglov, *Eur. Phys. J. B*, 2006, **51**, 293–300.
2 S. N. Bagaev, V. I. Dashkevich, V. A. Orlovich, S. M. Vatnik, A. A. Pavlyuk and A. M. Yurkin, *Quantum Electron.*, 2011, **41**, 189.
3 E. V. Alekseev, O. Felbinger, S. Wu, T. Malcherek, W. Depmeier, G. Modolo, T. M. Gesing, S. V. Krivovichev, E. V. Suleimanov, T. A. Gavrilova and L. D. Pokrovsky, *J. Solid State Chem.*, 2013, **204**, 59–63.
4 C. S. Lim, A. Aleksandrovsky, M. Molokeev, A. Oreshonkov and V. Atuchin, *J. Solid State Chem.*, 2015, **228**, 160–166.
5 P. Jena, S. K. Gupta, V. Natarajan, M. Sahu, N. Satyanarayana and M. Venkateswarlu, *J. Lumin.*, 2015, **158**, 203–210.
6 C. H. Chiu, M. F. Wang, C. S. Lee and T. M. Chen, *J. Solid State Chem.*, 2007, **180**, 619–627.
7 N. Garg, A. K. Mishra, H. K. Poswal, A. K. Tyagi and S. M. Sharma, *J. Solid State Chem.*, 2015, **229**, 164–172.
8 S. Schwung, D. Rytz, B. Heying, U. C. Rodewald, O. Niehaus, D. Enseling, T. Jüstel and R. Pöttgen, *J. Lumin.*, 2015, **166**, 289–294.
9 J. R. de Moraes, S. L. Baldochi, L. D. R. L. Soares, V. L. Mazzocchi, C. B. R. Parente and L. C. Courrol, *Mater. Res. Bull.*, 2012, **47**, 744–749.
10 T. Shimemura, N. Sawaguchi and M. Sasaki, *J. Ceram. Soc. Jpn.*, 2017, **125**, 150–154.
11 T. Shimemura, N. Sawaguchi and M. Sasaki, *J. Ceram. Soc. Jpn.*, 2016, **124**, 938–942.
12 L. Ma, Z. Xia, V. Atuchin, M. Molokeev, S. Auluck, A. H. Reshak and Q. Liu, *Phys. Chem. Chem. Phys.*, 2015, **17**, 31188–31194.
13 A. H. Reshak, Z. A. Alahmed, J. Bila, V. V. Atuchin, B. G. Bazarov, O. D. Chimitova, M. S. Molokeev, I. P. Prosvirin and A. P. Yelisseyev, *J. Phys. Chem. C*, 2016, **120**, 10559–10568.
14 A. K. Munirathnappa, D. Dwibedi, J. Hester, P. Barpanda, D. Swain, C. Narayana and N. G. Sundaram, *J. Phys. Chem. C*, 2018, **123**, 1041–1049.
15 W. R. Liu, C. W. Yeh, C. H. Huang, C. C. Lin, Y. C. Chiu, Y. T. Yeh and R. S. Liu, *J. Mater. Chem.*, 2011, **21**, 3740–3744.
16 C. S. Lim, A. Aleksandrovsky, M. Molokeev, A. Oreshonkov and V. Atuchin, *Molecules*, 2021, **26**, 7357.
17 C. S. Lim, A. Aleksandrovsky, M. Molokeev, A. Oreshonkov and V. Atuchin, *Crystals*, 2023, **13**, 362.
18 G. M. Kuzmicheva, A. V. Eremin, V. B. Rybakov, K. A. Subbotin and E. V. Zharikov, *Russ. J. Inorg. Chem.*, 2009, **54**, 854–863.

19 L. Li, Y. Su and G. Li, *Appl. phys. let*, 2007, **90**, 054105.
20 M. Gancheva, A. Naydenov, R. Iordanova, D. Nihtianova and P. Stefanov, *J. Mater. Sci.*, 2015, **50**, 3447–3456.
21 A. H. Ahmad and A. K. Arof, *Ionics*, 2004, **10**, 200–205.
22 N. Haldar, T. Mondal, T. Das, D. Sarkar, M. Pal and C. K. Ghosh, *CrystEngComm*, 2023, **25**, 3514–3527.
23 N. Haldar, T. Mondal, A. Dutta, D. Sarkar, U. K. Ghorai and C. K. Ghosh, *Appl. Phys. A: Mater. Sci. Process.*, 2023, **129**, 708.
24 L. Macalik, J. Hanuza and A. A. Kaminskii, *J. Mol. Struct.*, 2000, **555**, 289–297.
25 A. Jayaraman, S. K. Sharma and S. Y. Wang, *J. Raman Spectrosc.*, 1998, **29**, 305–312.
26 N. Dirany, E. McRae and M. Arab, *CrystEngComm*, 2017, **19**, 5008–5021.
27 N. Haldar, T. Mondal, T. Das, D. Sarkar, M. Pal and C. K. Ghosh, *CrystEngComm*, 2023, **25**, 3514–3527.
28 V. V. Atuchin, L. D. Pokrovsky, O. Y. Khyzhun, A. K. Sinelnichenko and C. V. Ramana, *J. Appl. Phys.*, 2008, **104**, 033518.
29 V. V. Atuchin, L. I. Isaenko, V. G. Kesler, Z. S. Lin, M. S. Molokeev, A. P. Yelisseyev and S. A. Zhurkov, *J. Solid State Chem.*, 2012, **187**, 159–164.
30 O. Y. Khyzhun, V. L. Bekenev, V. V. Atuchin, E. N. Galashov and V. N. Shlegel, *Mater. Chem. Phys.*, 2013, **140**, 588–595.
31 S. Mandal, C. K. Ghosh, D. Sarkar, U. N. Maiti and K. K. Chattopadhyay, *Solid State Sci.*, 2010, **12**, 1803–1808.
32 C. V. Ramana, V. V. Atuchin, L. D. Pokrovsky, U. Becker and C. M. Julien, *J. Vac. Sci. Technol., A*, 2007, **25**, 1166–1171.
33 C. V. Ramana, R. S. Vemuri, V. V. Kaichev, V. A. Kochubey, A. A. Saraev and V. V. Atuchin, *ACS Appl. Mater. Interfaces*, 2011, **3**, 4370–4373.
34 E. J. Rubio, V. V. Atuchin, V. N. Kruchinin, L. D. Pokrovsky, I. P. Prosvirin and C. V. Ramana, *J. Phys. Chem. C*, 2014, **118**, 13644–13651.
35 L. S. Cavalcante, F. M. C. Batista, M. A. P. Almeida, A. C. Rabelo, I. C. Nogueira, N. C. Batista, J. A. Varela, M. R. M. C. Santos, E. Longo and M. S. Li, *RSC Adv.*, 2012, **2**, 6438–6454.
36 G. Li, Y. Tian, Y. Zhao and J. Lin, *Chem. Soc. Rev.*, 2015, **44**, 8688–8713.
37 L. G. Van Uitert, *J. Lumin.*, 1984, **29**, 1–9.
38 A. Lecointre, A. Bessière, A. J. J. Bos, P. Dorenbos, B. Viana and S. Jacquart, *J. Phys. Chem. C*, 2011, **115**, 4217–4227.
39 A. K. Singh, S. K. Singh and S. B. Rai, *RSC Adv.*, 2014, **4**, 27039–27061.
40 W. Ran, H. M. Noh, S. H. Park, B. K. Moon, J. H. Jeong, J. H. Kim and J. Shi, *Sci. Rep.*, 2018, **8**, 5936.
41 X. Li, Z. Yang, L. Guan, J. Guo, Y. Wang and Q. Guo, *J. Alloys Compd.*, 2009, **478**, 684–686.
42 N. Haldar, T. Mondal, A. Dutta, D. Sarkar, U. K. Ghorai and C. K. Ghosh, *Appl. Phys. A: Mater. Sci. Process.*, 2023, **129**, 708.
43 N. Haldar, T. Mondal, T. Das, D. Sarkar, M. Pal, A. H. Seikh and C. K. Ghosh, *Mater. Adv*, 2024, **5**, 4480–4490.
44 M. Rai, G. Kaur, S. K. Singh and S. B. Rai, *Dalton Trans.*, 2015, **44**, 6184–6192.